



Copper Single Atoms Chelated on Ligand-Modified Carbon for Ullmann-type C–O Coupling

Vincenzo Ruta,^[a] Giovanni Di Liberto,^[b] Francesco Moriggi,^[a] Yurii P. Ivanov,^[c] Giorgio Divitini,^[c] Gianlorenzo Bussetti,^[d] Vincenzina Barbera,^[a] Mark A. Bajada,^[a] Maurizio Galimberti,^[a] Gianfranco Pacchioni,^[b] and Gianvito Vilé*^[a]

Cross-coupling reactions are of great importance in chemistry due to their ability to facilitate the construction of complex organic molecules. Among these reactions, the Ullmann-type C–O coupling between phenols and aryl halides is particularly noteworthy and useful for preparing diarylethers. However, this reaction typically relies on homogeneous catalysts that rapidly deactivate under harsh reaction conditions. In this study, we introduce a novel heterogeneous catalyst for the Ullmann-type C–O coupling reaction, comprised of isolated Cu atoms

chelated to a tetraethylenepentamine-pyrrole ligand that is immobilized on graphite nanoplatelets. The catalytic study reveals the recyclability of the material, and demonstrates the crucial role of the pyrrole linker in stabilizing the Cu sites. The work expands the potential of single-atom catalyst nano-architectures and underscores the significance of ligands in stabilizing metals in cationic forms, providing a novel, tailored catalyst for cross-coupling chemistries.

Introduction

Transition metal-catalyzed cross-coupling reactions are widely applied in organic synthesis for the formation of C–C, C–O, and C–N bonds.^[1–5] Among the best known and most exploited reactions, the Ullmann-type coupling allows the formation of C–O bonds from readily available phenols and aryl halides in the presence of a base (e.g., KOH, Cs₂CO₃, or K₂CO₃).^[5,6] This reaction, however, is characterized by the use of stoichiometric amount of homogeneous copper catalysts and bulky or toxic ligands to activate the catalytic system (Figure 1).^[6–8] On the one hand, homogeneous catalysts suffer from a variety of intrinsic issues, such as low stability and the difficulty to recover

and reuse the catalytic phase after reaction.^[10–13] Additionally, the use of bulky or toxic ligands can limit access to the catalytic site, leading to reduced reactivity, and/or pose hazards during their synthesis, use, and post-reaction disposal.^[14–16] One effective solution to circumvent these issues is the heterogenization of the active site, achievable through the anchoring of metals on solid supports.^[17,18] This approach offers a promising means of combining the advantages of homogeneous and heterogeneous systems, resulting in atom efficiency, uniformity of the active site, and prolonged stability.^[13,19,20]

To date, the Ullmann coupling reaction was studied in a heterogeneous configuration over copper nanoparticles supported on various carriers (e.g., magnetite,^[21] zeolites,^[22] carbon nanotubes,^[23] graphene oxide,^[24] and metal-organic frameworks^[25]). Among those, *sp*² carbon allotropes, such as graphene, carbon nanotubes, and graphite nanoplatelets (GNPs), offer the possibility to modulate the carrier surface chemistry through appropriate functionalization,^[26,27] thereby tailoring the local environment around the catalytic center to mimic the function of additives, ligands, or enzymes.^[16–19] To introduce functional groups on poorly reactive *sp*²-hybridized carbon surface, harsh conditions are generally employed.^[28,32–34] In this regard, the covalent grafting of pyrrole compounds is an alternative approach that has been recently developed,^[35] and it is based on a domino reaction made of the carbocatalytic oxidation of the pyrrole compound followed by Diels-Alder reaction between the GNPs carbonaceous surface and the pyrrole moiety.^[36,37] This approach allows the facile functionalization of the material, thereby circumventing the need for harsh conditions.

By extending the applicability of this strategy, we design herein a new heterogeneous catalyst for the Ullmann coupling reaction, merging single-atom catalysis with covalent pyrrole grafting. The catalyst (denoted as Cu@f-GNPs) features dispersed copper single atoms chelated onto the tetraethylene-

[a] Dr. V. Ruta, F. Moriggi, Dr. V. Barbera, Dr. M. A. Bajada, Dr. M. Galimberti, Prof. Dr. G. Vilé
 Department of Chemistry, Materials, and Chemical Engineering
 "Giulio Natta" Politecnico di Milano
 Piazza Leonardo da Vinci 32, IT-20133 Milano (Italy)
 E-mail: gianvito.vile@polimi.it

[b] Dr. G. Di Liberto, Prof. Dr. G. Pacchioni
 Department of Materials Science
 Università degli Studi di Milano-Bicocca
 Via Roberto Cozzi 55, IT-20125 Milano (Italy)

[c] Y. P. Ivanov, Dr. G. Divitini
 Electron Spectroscopy and Nanoscopy
 Italian Institute of Technology
 Via Morego 30, IT-16163 Genova (Italy)

[d] Dr. G. Bussetti
 Department of Physics
 Politecnico di Milano
 Piazza Leonardo da Vinci 32, IT-20133 Milano (Italy)

Supporting information for this article is available on the WWW under <https://doi.org/10.1002/cssc.202301529>

© 2023 The Authors. ChemSusChem published by Wiley-VCH GmbH. This is an open access article under the terms of the Creative Commons Attribution License, which permits use, distribution and reproduction in any medium, provided the original work is properly cited.

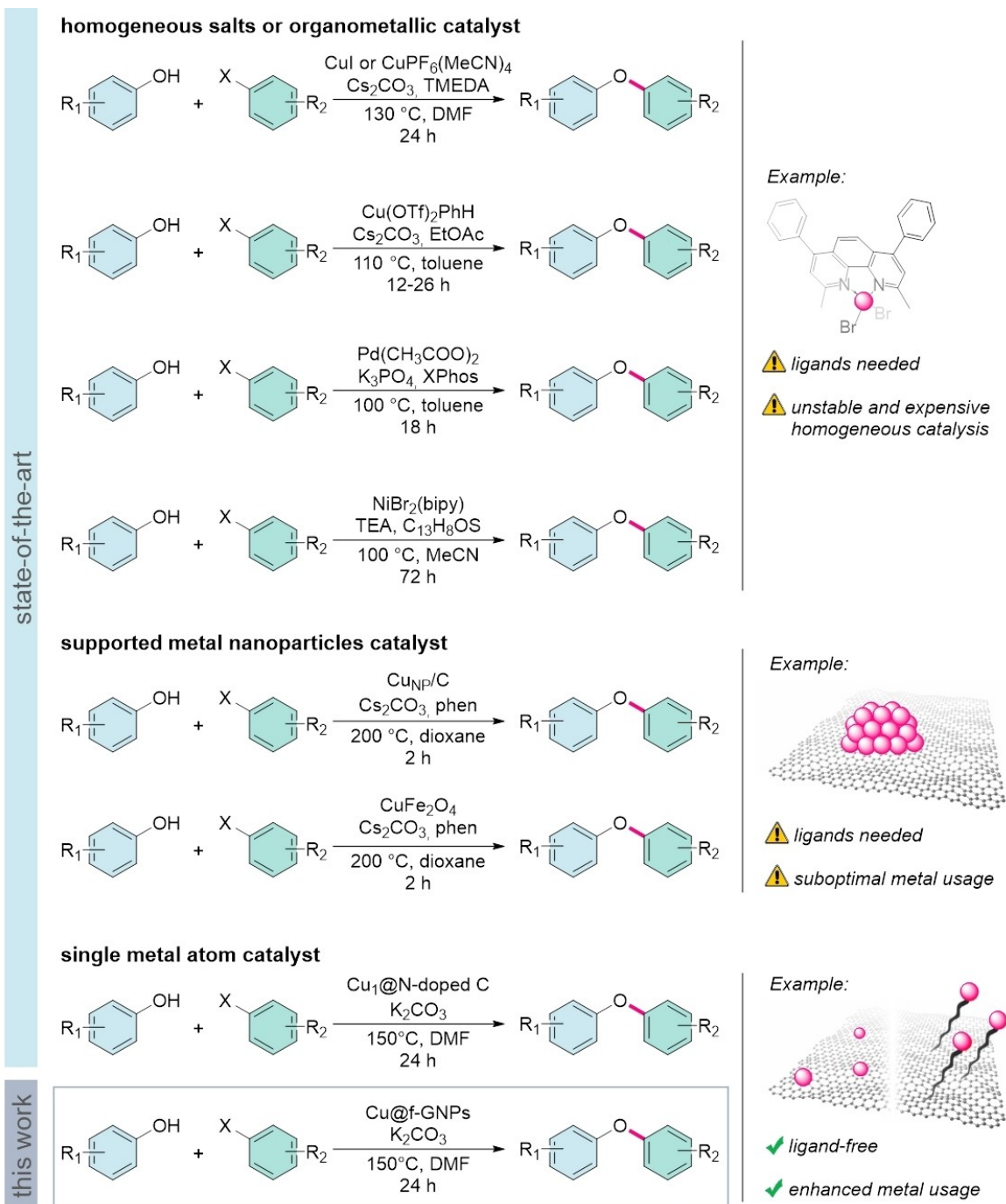


Figure 1. State-of-the-art on Ullmann-type C–O cross coupling reactions. Abbreviations: Xphos = 2-Dicyclohexylphosphino-2',4',6'-triisopropylbiphenyl; Tf = triflyl group; phen = 1,10-Phenanthroline; TEA = triethylamine; DMF = N,N-dimethylformamide; MeCN = acetonitrile.

pentamine-pyrrole functionalized GNPs. A comprehensive investigation of the properties of the catalyst was carried out with the aim of establishing a correlation between its structure and reactivity. The newly developed synthetic method offers several advantages over established procedures, including a simpler and greener route for preparing single-atom catalysts with high yield, and the elimination of any homogeneous additives during the C–O coupling Ullmann reaction.

Results and discussion

Preparation and characterization of the single-atom catalyst.

The chelation of the isolated copper atoms on the ligand-functionalized graphene has been performed by following the procedure summarized in Figure 2a. Firstly, the pyrrole compound, *N*¹-(2-aminoethyl)-*N*²-(2-((2,5-dimethyl-1*H*-pyrrol-1-yl)ethyl)amino)ethyl)ethane-1,2-diamine (TEPAP), was prepared through the Paal-Knorr reaction, by reacting the polyamine, *N*¹-

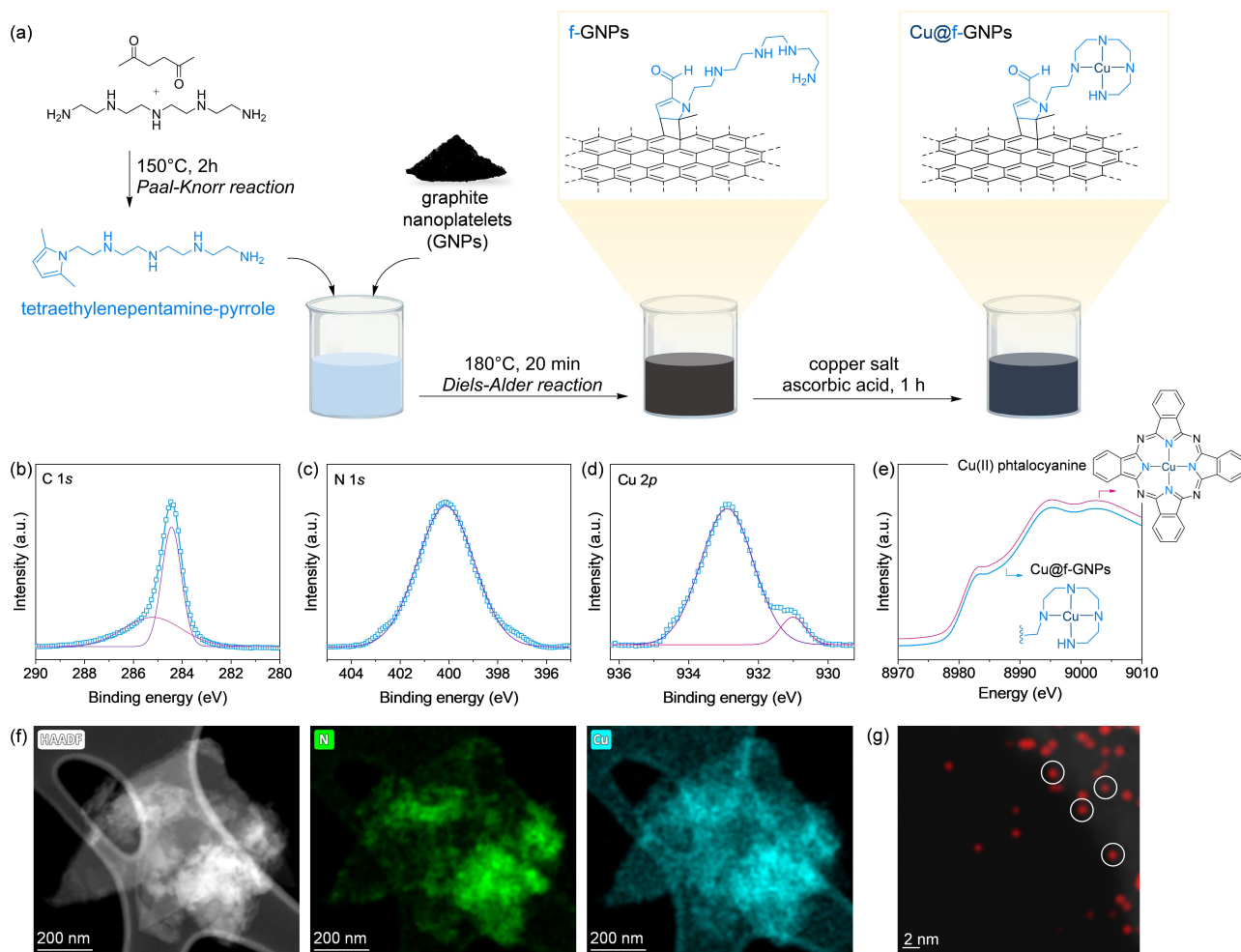


Figure 2. Schematic representation of the synthesis of the Cu@f-GNPs catalyst (a); C 1s (b), N 1s (c), and Cu 2p (d) XPS core level spectra of Cu@f-GNPs; XANES profile of Cu@f-GNPs and of a reference Cu^{II} phthalocyanine (e); High-resolution HAADF-STEM of Cu@f-GNPs (f). EDX map of Cu overlaid obtained from the high-resolution HAADF-STEM image of the Cu@f-GNPs catalyst with different layer thickness (g).

(2-aminoethyl)-*N*²-(2-((2-aminoethyl)amino)ethyl)ethane-1,2-diamine, with 2,5-hexanedione. At this stage, a domino reaction occurs: the carbo-catalyzed oxidation of the pyrrole is followed by a Diels-Alder cycloaddition, leading to covalent functionalization of the carbonaceous support with TEPAP. Once the f-GNPs adduct is obtained, the decoration with copper is performed via ion exchange. A catalyst made of Cu@GNPs was also prepared as a reference sample, by simple ion exchange of the pure GNPs carrier (see the Materials and Methods section for further experimental details). The sustainability of our newly developed catalytic protocol is intrinsic to the catalyst structure. The presence of the polyaminic moiety on the catalyst surface avoids the use of external ligands, ubiquitous in many heterogeneous and homogeneous protocols of this reaction, leading to easier downstream operations to purify and isolate reaction products. The environmental advantages of preparing our single-atom catalyst were further demonstrated through a detailed assessment of green metrics applied to the aforementioned synthetic protocol. The results of this study, summarized in Table S1 in the Supporting Information, indicate that the adopted synthetic protocol is inherently more environmentally

sustainable in comparison to the synthesis of a conventional Cu-based catalyst. The higher value of reaction mass efficiency suggests nearly complete conversion of the reactants into the final product, while lower values for process mass intensity and solvent intensity respectively highlight the reduced impact of the total mass input in our synthesis and a smaller contribution of solvents in our protocol.

The obtained catalysts were subjected to inductively coupled plasma-optical emission spectroscopy (ICP-OES) to determine their Cu loading, which was found to be 4.2 wt% for Cu@f-GNPs, and 4.7 wt% for Cu@GNPs (Table 1). CHN analysis was also employed to determine the exact carbon-to-nitrogen (C/N) ratios in the obtained catalysts, as presented in Table 1. Specifically, the C/N ratio of GNPs and Cu@GNPs was found to be approximately 135.0, whereas the ratio reduced to 25.7 in the presence of a ligand, indicating that the catalyst preserved its desired elemental composition and functional group densities after copper immobilization. Notably, the observed variations in the nitrogen values in the TEPAP-functionalized materials were consistent with the anticipated values, thereby

Table 1. Elemental composition and surface area values of the prepared materials.

Entry	Catalyst	C ^a (wt %)	H ^a (wt %)	N ^a (wt %)	C/N ratio (–)	Cu ^b (wt %)	S _{BET} ^c (m ² g ^{–1})
1	GNPs	93.6	0.13	0.69	135.7	–	244
2	f-GNPs	88.9	0.41	3.46	25.7	–	48.5
3	Cu@GNPs	89.2	0.11	0.66	135.2	4.7	40.5
4	Cu@f-GNPs	85.2	0.12	3.31	25.7	4.2	43.8

^aCHN values; ^bICP-OES values; ^cBET surface area from the N₂ isotherms collected at 77 K.

confirming the successful functionalization of graphite nanoplatelets.

N₂ physisorption experiments were performed to assess the surface area of the samples. After functionalization of GNPs with the TEPAP ligand and Cu immobilization, a significant reduction in the surface area was observed (from 244 m²g^{–1} in GNPs to 48.5 m²g^{–1} in f-GNPs), consistent with the ligand occupying surface sites on the graphitic layer. However, the introduction of Cu sites had a negligible effect on the surface area (the S_{BET} is 43.8 m²g^{–1}, similar to that of f-GNPs), indicating a well-dispersed metal distribution and the limited interaction of metal aggregates that could decrease the surface area (Table 1). Interestingly, the BET surface area of Cu@GNPs was found to be 40.5 m²g^{–1}, suggesting the presence of metal aggregates on the bare GNPs carrier, that results in a decrease of the surface area. We attributed the decrease in surface area to the formation of copper nanoparticles in the Cu@GNPs sample (refer to Figure S1 in the Supporting Information for evidence of nanoparticle formation). This formation is prevented in the presence of the polyaminic linker, which can stabilize the metal in isolated form (*vide infra*). Notably, the similar textural properties of Cu@GNPs and Cu@f-GNPs indicate that the observed catalytic differences cannot be attributed to surface area alone but are likely associated with the variable coordination of the metal sites in the samples.

X-ray powder diffraction (XRD) analysis was performed to assess phase purity, crystallinity, and composition of the materials. Figure S2 in the Supporting Information shows the diffractograms obtained for the pristine GNPs, f-GNPs, Cu@GNPs, and Cu@f-GNPs. The peak observed at around 26° corresponds to (002) planes of the graphite carbon support. The relative peak intensities remain unchanged after functionalization with TEPAP, and no new peaks appear. Similarly, no changes are observed following the copper decoration step, which suggests that the copper is highly dispersed on the support.

To evaluate the oxidation state and valence of the elements composing the catalysts, X-ray photoelectron spectroscopy (XPS) was performed on the copper-containing samples. Figure 2 includes the C 1s, N 1s, and Cu 2p profiles of Cu@f-GNPs. In particular, the C 1s spectrum (Figure 2b) shown two components at 284.3 ± 0.1 eV and 285.2 ± 0.1 eV, which are identified with the sp² and sp³ components of C atoms.^[38] Similarly, the deconvoluted N 1s spectrum of Cu@f-GNPs (Figure 2c) features a peak (399.0 eV) assigned to Cu–N species.^[39]

By analyzing only the photoemission peaks, the Cu 2p XPS spectrum (Figure 2d) shows the characteristic peak of Cu^{II} 2p_{3/2} (932.8 eV) in Cu@f-GNPs, probing the strong chelation of Cu with surrounding N atoms in the TEPAP ligand.^[40] A shoulder at 931.0 eV is also visible in the line shape, compatible with the partial presence of Cu^I.^[41] X-ray absorption near edge spectroscopy (XANES) (Figure 2e) confirmed these results and showed the presence of Cu^{II} in the material, as seen from the adsorption edge of our catalyst similar to that of Cu^{II} phthalocyanine. Moreover, the similarity in the XANES profiles between the Cu^{II} phthalocyanine and the Cu@f-GNPs (as shown in Figure 2e), along with the large difference to the XANES spectra of reference Cu oxides and metals (as depicted in Figure S3 in the Supporting Information), indicates a local coordination environment where Cu is chelated to N atoms. To further prove the isolated nature of the Cu catalytic sites, the analysis of the extended X-ray absorption fine structure spectra was performed (Table S2, Supporting Information), showing the absence of Cu–Cu pairs scattering contribution; moreover, the metal atom results to be surrounded by four low-valent neighboring atoms, consistently with XPS and XANES data, at an average distance of 1.9 Å. For comparative purposes, the Cu 2p XPS analysis was also performed on the Cu@GNPs sample (Figure S4, Supporting Information), detecting oxidic Cu^{II} sites centered at 933.4 eV. Density Functional Theory (DFT) was applied to obtain better insights into the structure. The organic linker has, in fact, four terminal nitrogen atoms, each of which can be saturated by a hydrogen atom or have a formal negative charge. Therefore, the ligand can adopt different oxidation states depending on the number of hydrogen atoms bonding to the N-species. This affects the strength of the interaction between the Cu atom and the ligand ring. The structures of the four catalysts are shown in Figure S5. Indeed, all DFT calculations are performed by imposing a net charge of the system equal to zero, and the electron density is self-consistently optimized. The formal oxidation state of the ligand ranges from 0 to –IV, resulting in a formal oxidation state of Cu ranging from 0 to +IV.

The presence of isolated copper sites was finally visualized via microscopy. Aberration-corrected high-resolution scanning transmission electron microscopy (HRSTEM) combined with energy dispersive X-ray (EDX) analysis of the catalytic materials showed the absence of copper-based nanoparticles in Cu@f-GNPs (Figure 2f, left). In addition, the EDX N and Cu elemental maps together with high-angle annular dark-field (HAADF) STEM image (Figure 2f, center and right) corroborated the

homogeneous distribution of both the polyaminic ligand and metal phase throughout the carbonaceous support. Finally, the high magnification of EDX map of Cu overlaid obtained from the HAADF-HRSTEM image of the Cu@f-GNPs catalyst with different layer thickness acquired with 0.8 Å aberration corrected electron probe (Figure 2g) shows the isolated metals, marked by the distant red dots, on the carbon carrier. The half wide of the Cu signal (at the distant red dots) is about 6 Å which suggests the presence of the single Cu atoms assuming delocalization of the EDX signal, and possible atom mobility during acquisition.

Catalytic investigations and molecular understanding. The heterogeneous Cu@f-GNPs catalyst was applied in the Ullmann-type C–O coupling reaction between phenol and bromobenzene (Table 2). In a first trial, the optimization of the reaction was performed through studying the impact of: (i) the reaction solvent; (ii) the type of base; (iii) the amount of catalyst, on the conversion and selectivity of the opted reaction, and HPLC analysis was used to quantify such metrics. For the solvent screening, we decided to test two high-boiling solvent, namely DMF and DMSO, because literature data suggested that high temperatures were necessary to activate any Cu-based catalyst.^[4] When DMSO was employed as the reaction solvent, the diphenyl ether product was not observed (Entry 1). Instead, using DMF, a minimal product formation was detected (the rate of product formation was 17 mmol_{prod} mol_{Cu}⁻¹ h⁻¹) likely because of the increase of solvent polarity with respect to DMSO (Entry 2). The effect of the base was then investigated, demonstrating that weaker bases, *i.e.*, K₂CO₃ (Entry 3) and Cs₂CO₃ (Entry 4), were more effective for the reaction (rates of 201 and 155 mmol_{prod} mol_{Cu}⁻¹ h⁻¹, respectively). On the other hand, stronger bases like NaOH (Entry 5) led to a less efficient product formation (60 mmol_{prod} mol_{Cu}⁻¹ h⁻¹), due to the enhancement of competitive side-reactions. Finally, by screening the amount of catalyst employed in the reaction, we

showed that a higher amount of Cu (Entries 6 and 7) dropped the reaction rate, due to an enhanced substrate conversion but lower selectivity for the biphenyl ether.

A number of control experiments were also conducted. The first of such highlighted the importance of copper for the Ullmann coupling reaction, since no product was observed using TEPAP-functionalized GNPs without Cu (Entry 8). A second investigation regarding the role of the TEPAP linker was also carried out. In this case, the catalyst bearing Cu sites deposited on 'bare' GNPs (*i.e.*, without the polyamine linker) was employed for the reaction (Entry 9). Data obtained from this experiment showed that the latter catalyst provided a good substrate conversion (81%) but a lower selectivity for the desired biphenyl ether (21%), leading to a reaction rate of only 20 mmol_{prod} mol_{Cu}⁻¹ h⁻¹.

To gain a better understanding of the effect of temperature on the rate of biphenyl ether production, the catalytic reaction was studied at various temperatures, ranging from 90 to 150 °C (Figure 3a). From this investigation, it was evident that higher values of temperature were required in order to activate the catalyst and drive the reaction towards biphenyl ether formation. In particular, a maximum reaction rate of 201 mmol_{prod} mol_{Cu}⁻¹ h⁻¹ was obtained at 150 °C. To elucidate the stability of the heterogeneous catalytic system at this temperature, a kinetic profile of the coupling reaction was also carried out. The outcome of this study, which is summarized in Figure 3b, depicts the increasing product formation during the 24 h reaction period, reaching a maximum of 0.12 mmol of biphenyl ether by the end of the process. We also carried out post-catalysis characterization of the material following the 24-hour experiment depicted in Figure 3b. Primarily, XRD analysis (Figure S6) revealed the absence of reflections at high 2θ values corresponding to metallic copper. Additionally, XPS was employed to investigate whether the reaction conditions had an impact on the catalyst's structure. After the coupling

Table 2. Optimization study for the Ullmann coupling reaction.

Entry	Catalyst	Catalyst mass	T (°C)	Base	Solvent	Rate ^a (mmol _{prod} mol _{Cu} ⁻¹ h ⁻¹)
1	Cu@f-GNPs	8 mg	120	K ₂ CO ₃	DMSO	0
2	Cu@f-GNPs	8 mg	120	K ₂ CO ₃	DMF	17
3	Cu@f-GNPs	8 mg	150	K ₂ CO ₃	DMF	201
4	Cu@f-GNPs	8 mg	150	Cs ₂ CO ₃	DMF	155
5	Cu@f-GNPs	8 mg	150	NaOH	DMF	60
6	Cu@f-GNPs	24 mg	150	K ₂ CO ₃	DMF	104
7	Cu@f-GNPs	40 mg	150	K ₂ CO ₃	DMF	37
8	f-GNPs	8 mg	150	K ₂ CO ₃	DMF	0
9	Cu@GNPs	8 mg	150	K ₂ CO ₃	DMF	20

^aProduct mmol calculated from HPLC data, using a calibration curve of the diphenyl ether.

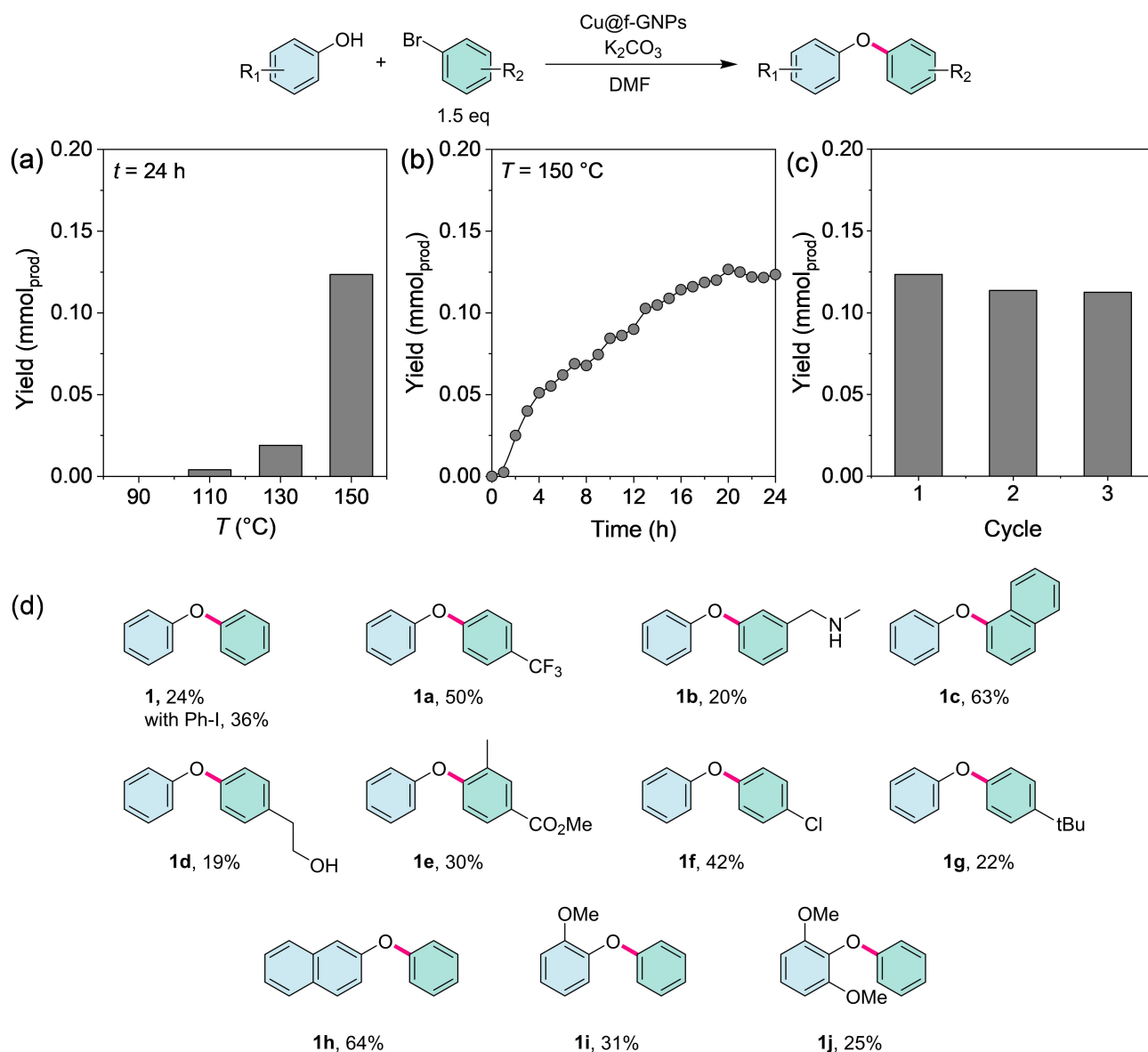


Figure 3. Influence of temperature (a) and reaction time (b) for the heterogeneous Ullmann coupling reaction over Cu@f-GNPs. Reaction conditions: phenol (0.5 mmol, 0.25 mM), bromobenzene (0.75 mmol), catalyst (8 mg), K₂CO₃ (1 mmol), DMF (2 mL). The mass of product is obtained based on HPLC analysis, using a calibration curve of the diphenyl ether. (c) Recycling test for Cu@f-GNPs catalyst at 150 °C for 24 h. (d) Substrate scope for the Ullmann-type C–O coupling reaction. The yields reported are obtained via NMR using dibromomethane as internal standard.

reaction, the prominent peak at 932.8 eV, attributed to N-coordinated Cu^{II} species,^[42,43] remained evident (Figure S6). To further prove the stability, and elucidate the reusability of our catalyst, a recyclability test composed of 3 consecutive reactions was performed (Figure 3c). The outcome of this study demonstrated the optimal reuse of our catalyst, supported by negligible leaching of Cu in the reaction solution evidenced by ICP-OES analysis.

Finally, to evaluate the flexibility of our protocol towards different functional groups, and further explore the reactivity of the novel catalytic system, differently decorated phenols and aryl bromides were tested. At first, we evaluated the reactivity of different aryl halides, testing in the model reaction chlorobenzene, iodobenzene, and fluorobenzene as electro-

philic partner, affording the biarylether product **1**. From these tests, the improved reactivity of iodobenzene with respect of brominated congener has been elucidated (36 and 24% yield, respectively), while fluoro- and chlorobenzene resulted to be inactive towards the C–O coupling, due to the two halides worst nature as leaving group. Regarding the aryl bromide scope, both electron withdrawing and electron donating groups were well supported, as demonstrated by the trifluoromethyl substituent in compound **1a** (50% yield), and the aromatic condensed core of 1-Br-naphtalene **1c** (63% yield), respectively, with a major preference for electron-donating substituents. Indeed, alkylic substituents present in compound **1b**, **1d**, and **1g** resulted in diminished yields, due to the minor electronic effects (20%, 19%, and 22% yield, respectively). The trend is

confirmed by the test of other electron-deficient aryl bromides **1e** (30% yield) and **1f** (42% yield), decorated with strong electron-withdrawing substituent. Stronger electron donating groups on the phenol moiety, in both the *ortho* and *para* positions, e.g., condensed system of 2-naphthol **1h** (64% yield), the methoxy moiety in guaiacol **1i** (31% yield), and the double methoxy substituent in compound **1j** (25% yield), lead to enhanced product formation, with the latter presenting a decreased reaction performance due to the possible steric hindrance of the two oxygenated groups. Thus, this difference appears to be related not only to the intensified electron density on the oxygen atom of phenol, stemming from stronger electron donating groups, but also to the bulkiness of the compound(s). This in-turn affects the nucleophilic attack of the phenols on the Cu center, and ultimately the rate of the reaction. The combined interplay of the electronic and geometric effects of the compounds on the catalytic efficiency are

well displayed in Figure 3c, where a quasi-linear correlation between the electron density normalized by the molecular diameter, and the product yield is observed. We finally compared the reactivity of our system with other catalysts (Table S3, Supporting Information). The excellent performance of Cu@f-GNPs compared to state-of-the-art materials highlights the significance of including ligands in Ullmann C–O type catalytic protocols and paves the way for further catalyst design optimization by combining metal and ligand catalysis in a single, heterogeneous material.

Theoretical calculations were employed at this step to rationalize the catalytic cycle (Figure 4a). The first step of the Ullmann coupling is the interaction between phenol and copper, forming a cuprate-like compound. Figure 4b shows the optimized structures and the calculated energies. We can observe that there is a clear trend between the free formation energy of the adduct and the nature of the catalyst. Indeed, as the metal

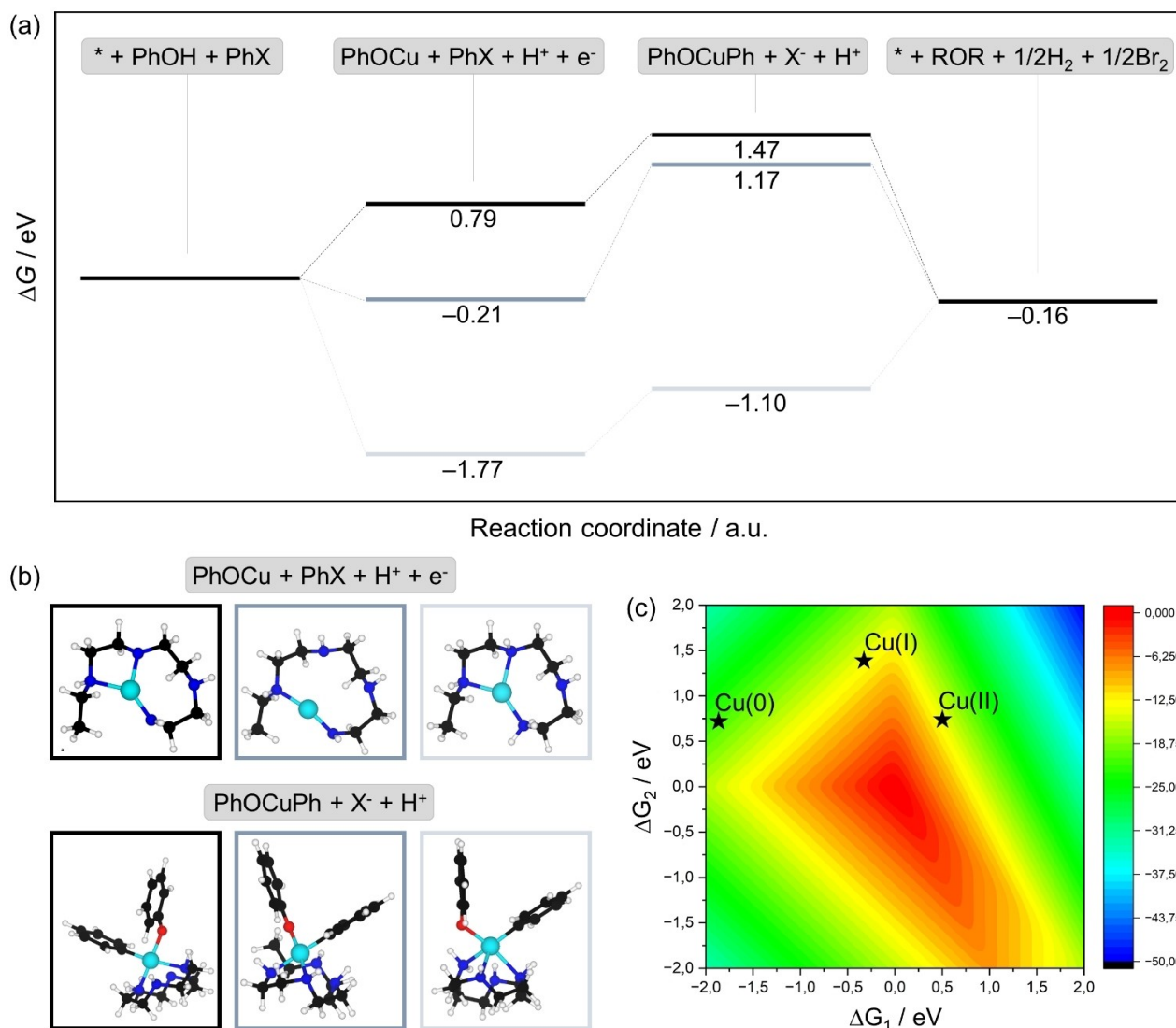
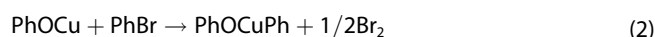
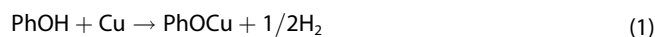


Figure 4. Gibbs free energy profiles of different active surfaces, with isolated metals having Cu⁰ (blue), Cu^I (light blue), and Cu^{II} (black) valence state (a). Optimized structures of possible PhOCu and PhOCuPh intermediates (b). Predicted reaction rates based on a kinetic model, for three different copper valence states (c). Light blue: Cu; blue: N; red: O; black: C; white: H. The entropic and zero-point energy contributions of reactants and products in standard condition are reported in Table S4.

binds a negatively charged matrix, it is less prone to accept further electronic density from PhOX to form PhOCu. The next step of the reaction is the coupling with PhBr, forming a cuprate while binding PhO⁻ and Ph⁻ units simultaneously. Figure 4b shows the optimized structures and Gibbs formation free energies. We first observe that when Cu is embedded in a strongly negatively charged cavity, not only is it not prone to form PhOCu, but it is also unable to bind both PhO⁻ and Ph⁻ moieties at the same time. This result is not surprising since it corresponds to an unrealistic picture. On the contrary, a Cu atom that is formally neutral is again too reactive, forming very stable adducts. Based on the calculated Gibbs formation free energies, we constructed reaction profiles reported in Figure 4a. Figure 4c allows us to appreciate the different behavior of Cu⁰ compared to Cu^I or Cu^{II}. In the first case, the catalyst is very reactive and strongly binds the PhO⁻. The next reaction steps need to climb a very large overall reaction barrier of 1.77 eV. In the presence of Cu^I, the formation of the cuprate is exergonic ($\Delta G = -0.21$ eV), and the coupling with PhX needs to overcome a large barrier of 1.38 eV, as the formation free energy of PhOCuPh is 1.17 eV. Cu^{II} is less reactive, and the formation of the cuprate is endergonic by 0.79 eV. The coupling with PhX is still endergonic with a further barrier of 0.68 eV. In summary, the reactivity of Cu⁰ is very different from that of Cu^I and Cu^{II}. The latter two are characterized by a similar behavior, with the Cu^{II} requiring overcoming two barriers that are lower than that needed for Cu^I.

To gain a more quantitative estimate of the catalytic activity of the different SACs layers, we constructed a simple kinetic model based on reaction profiles and calculated reaction energies. The reaction was modeled according to the following steps (1–3):



Assuming we work under standard conditions and apply the steady-state approximation for the PhOCu and PhOCuPh intermediates,^[44,45] we can write the rates as follows (4–5):

$$v_{\text{PhOCu}} = 0 = k_1\theta_{\text{Cu}}e^{-\frac{\beta\Delta G_1}{k_bT}} + k_{-2}\theta_{\text{PhOCuPh}}e^{\frac{(1-\beta)\Delta G_2}{k_bT}} = k_{-1}\theta_{\text{PhOCu}}e^{-\frac{(1-\beta)\Delta G_1}{k_bT}} + k_2\theta_{\text{PhOCu}}e^{-\frac{\beta\Delta G_2}{k_bT}} \quad (4)$$

$$v_{\text{PhOCuPh}} = 0 = k_2\theta_{\text{PhOCu}}e^{-\frac{\beta\Delta G_2}{k_bT}} = k_{-2}\theta_{\text{PhOCuPh}}e^{\frac{(1-\beta)\Delta G_2}{k_bT}} + k_3\theta_{\text{PhOCu}}e^{\frac{(1-\beta)(\Delta G_1+\Delta G_2)}{k_bT}} \quad (5)$$

where θ_{Cu} , θ_{PhOCuPh} , and θ_{PhOCu} represent the fraction of catalytic sites occupied by the free catalyst, PhOCu, and PhOCuPh, respectively. On the other hand, β is the symmetry factor of the reaction barriers, and a typical value of it adopted in other studies is 0.5. If we consider that $1 = \theta_{\text{Cu}} + \theta_{\text{PhOCuPh}} + \theta_{\text{PhOCu}}$, and that the reaction rate can be

written as: $v = k_3\theta_{\text{PhOCuPh}}e^{\frac{(1-\beta)(\Delta G_1+\Delta G_2-0.16\text{eV})}{k_bT}}$, we can find an approximate expression of the reaction rate as a function of ΔG_1 and ΔG_2 . For simplicity, we approximate all pre-exponential terms as equal to 1. This leads to the following expression of the reaction rates (6):

$$v = \frac{e^{\frac{(1-\beta)(\Delta G_1+\Delta G_2-0.16\text{eV})}{k_bT}}}{1 + e^{\frac{\Delta G_1+\beta\Delta G_2}{k_bT}} + e^{\frac{\Delta G_2}{k_bT}} + e^{\frac{\beta\Delta G_1+\Delta G_2}{k_bT}} + e^{\frac{\Delta G_1+\Delta G_2}{k_bT}} + e^{\frac{(1+\beta)\Delta G_1+\Delta G_2}{k_bT}}} \quad (6)$$

Based on this analysis, Figure 4c shows the behavior of the calculated reaction rate as a function of ΔG_1 and ΔG_2 . We observe that both oxidized Cu single atoms are predicted to be more active than Cu⁰, and Cu^I offers better performance than Cu^{II}.

Conclusions

In conclusion, we have developed a novel single-atom catalyst that is well tailored for catalyzing the Ullmann C–O coupling reaction. The material was prepared using a mild, multistep reaction protocol, and was characterized using several techniques. The battery of methods applied allowed us to elucidate the structure and properties of the Cu-based carbonaceous materials, featuring isolated Cu atoms chelated on the adsorbed pyrrole ligand. The application of the heterogeneous catalyst for the Ullmann coupling reaction was successful, demonstrating the high performance of the devised system (evidenced by the kinetic test conducted at 150 °C for 24 h) and the substrate versatility (evidenced by the aryl bromide and phenol scopes). The polyamine linker was identified as a crucial component for immobilization of the isolated metal atoms. Moreover, the experimental evidence highlighted that the polyamine moiety stabilizes reaction intermediates, thereby lowering the energetics of, and facilitating, the coupling reaction. Overall, the study allowed us to explore the potential of a novel family of Cu-based single-atom catalysts for a highly relevant reaction protocol, offering a greener and more sustainable outlook for this class of synthetic transformations.

Materials and methods

Catalyst preparation. The tetraethylenepentamine-pyrrole (TE-PAP) linker was first synthesized through a Paal-Knorr reaction, in which a diketone was reacted with a primary amine to form a mono *N*-substituted pyrrole. Tetraethylenepentamine (Sigma Aldrich, >95% purity, 3.7 g, 20 mmol) and 2,5-hexanedione (Sigma-Aldrich, >99% purity, 2.3 g, 20 mmol) were mixed in bulk conditions in a flask and heated under vigorous stirring at 150 °C for 2 h. To prepare TE-PAP-functionalized graphite nanoplatelets (f-GNPs), graphite nanoplatelets (10 g) were poured in a flask along with TE-PAP (1.5 g, 13 wt%) and acetone (100 mL). After sonicating the dispersion for 20 min, the solvent was evaporated, and the dried powder was then heated at 180 °C for 2 h. Extraction with acetone was performed overnight to

remove unreacted pyrrole compounds. Cu grafting on f-GNPs was performed by mixing f-GNPs (1.0 g) with copper(II) acetate (Sigma Aldrich, 99% purity, 1 mmol, 0.2 g), in 40 mL of water. After 45 min of continuous stirring, an aqueous solution of ascorbic acid (Sigma Aldrich, 99% purity, 34 mmol, 6 g, dissolved in 80 mL of water), was added. After this addition, the mixture was kept under stirring for 1 h. The resulting mixture was filtered, yielding a black powder that was washed with both water and methanol. The product was then dried in an oven at 80 °C for 1 h. Cu@GNPs were prepared with the same approach by following the same procedure, wherein a similar quantity of pristine GNPs (1.0 g) was used in place of f-GNPs.

Catalyst characterization. Elemental analysis was performed using a Costech ECS4010 elemental analyser which allows the simultaneous quantification of C, H, N, and S. Results are the average of 4 tests performed on the same sample. Inductively coupled plasma optical emission spectroscopy (ICP-OES) analysis was performed using a Horiba Ultra 2 instrument equipped with photomultiplier tube detection. X-ray photoelectron spectroscopy (XPS) was performed in an ultra-high vacuum chamber with the base pressure of 2×10^{-10} Torr, and a non-chromatized Mg K α source (photon energy = 1253.6 eV) at normal emission and room temperature.^[46] Photoelectrons were collected by a 150 mm hemispherical analyzer (SPECS GmbH) with a pass energy of 20 eV for high-resolution spectra and 40 eV for wide spectra. Because this apparatus does not consent to analyze samples in powder form, pellets were made using a manual hydraulic press. Wide-angle X-ray powder diffraction (XRD) was performed on an automatic Bruker D8 Advance Diffractometer with a nickel-filtered Cu K α radiation (1.5406 Å wavelength). The doubled glancing angle (2θ) was set from 5° to 80°. For microscopy analysis, the materials were dispersed on TEM grids and analysed in a ThermoFisher Spectra300 (S)TEM microscope operated at 60 kV. The EDX signal was acquired on a dual-X detector with a total collection solid angle of 1.76 sr. Data were processed using Velox. X-ray absorption spectroscopy (XAS) experiments were conducted at the SuperXAS beamline of the Swiss Light Source at the Paul Scherrer Institute in Villigen, Switzerland. The radiation emitted by a 2.9 T bending magnet was collimated using a Si-coated collimating mirror at 2.9 mrad, which also served to reject higher harmonics through a channel-cut monochromator. The spot size of 1.0 mm \times 0.2 mm on the sample was achieved using a Rh-coated toroidal mirror. The beamline offers an X-ray flux of 6×10^{11} photons s⁻¹ and an energy bandwidth of 1 eV at the Cu K-edge. XAS spectra of samples pressed into pellets were collected in transmission mode using a 20 cm long ionization chamber filled with 1 bar of nitrogen. Spectra were collected with a scanning speed of 1 Hz (quick-scanning mode), and 300 spectra were averaged per sample. The Fourier transform (FT) of the k^3 -weighted EXAFS oscillations and $k^3\chi(k)$ from k -space to r -space was conducted in the range of 3–13 Å⁻¹ for curve fitting analysis.

Catalytic tests. The phenol (1 equiv, 0.5 mmol, 0.25 mM), aryl bromide (1.5 equiv, 0.75 mmol), and base (2 equiv, 1 mmol) were dissolved in a glass tube in 2 mL of solvent, and the catalyst (8 mg) was added. The tube was sealed and heated in an oil bath at the desired temperature, from 90 to 150 °C, for

24 h. For analysis, an aliquot (50 μ L) of the reaction mixture was diluted in acetonitrile (MeCN, 3 mL) and analyzed via high-performance liquid chromatography (HPLC), using an Agilent 1200 instrument, equipped with an ultraviolet-visible detector (G1315D) set at 210 nm. Samples (10 μ L) were injected directly onto a 250 mm \times 4.6 mm HypersilGOLD™ 5 μ m \times 175 Å column purchased from Thermo-Fisher. The mobile phase was comprised of a 60:40 MeCN:H₂O mixture with a total flow rate of 0.7 mL min⁻¹ at 40 °C. When conducting either analysis, 45 min of equilibration was required before the first sample injection. Initially, starting materials were analyzed separately to identify their retention times on the chromatogram; limiting reagent and product calibration curves were carried out, to calculate conversion and yields; selectivity is calculated by the peak area method. For the substrate scope, the reaction mixture is filtered to separate the catalyst, diluted in icy water (5 mL) and extracted with diethyl ether (5 mL); the organic phase is evaporated, re-dissolved in CDCl₃ and analyzed by means of NMR spectroscopy. NMR spectra both ¹H and ¹³C were collected on a Bruker 400 MHz (100 MHz) spectrometer.

DFT calculations. Theoretical calculations were performed using the Density Functional Theory (DFT) implemented in the Vienna *ab initio* Simulation Package (VASP) code.^[47] The Perdew-Burke-Ernzerhof parametrization of the exchange and correlation functional was adopted.^[48] The valence electrons were expanded using a set of plane waves by adopting a kinetic cutoff of 400 eV, whereas core electrons were treated with pseudopotentials using the Projector Augmented Approach.^[49,50] Dispersion forces were accounted for by employing Grimme's D3 scheme.^[51,52] Electronic self-consistent calculations were considered converged by setting a threshold of 10⁻⁵ eV, while geometry optimization was performed within the Conjugate Gradient algorithm, and a force threshold of 10⁻² eV Å⁻¹ was applied.

We performed PBE0 single-point calculations on top of PBE-optimized structures. This allows for the improvement of the description of the electronic structure of the systems with an acceptable computational effort. We approximated the catalyst by considering the active phase, *i.e.*, taking the metal atom embedded in the carbon ring with four nitrogen coordinating atoms. The presence of the graphene support was neglected. This assumption can be considered acceptable, assuming that only Cu atoms are active for the Ullmann coupling. Gibbs free energy profiles were calculated within the Nørskov thermochemistry approach, assuming standard conditions,^[53] and Gibbs free energies were obtained by adding the entropic contribution to the calculated DFT energies.^[54–56] The entropy of solid-state species was neglected, and that of reactants and products was taken from International Tables.^[57] The zero-point energy correction was always considered, working in a harmonic fashion. Table S4 in the Supporting Information reports the working entropic and zero-point contributions for the different structural coordination of Cu single atoms. As an energy reference, we used $\frac{1}{2}$ H₂ and $\frac{1}{2}$ Br₂ rather than H⁺ and Br⁻ according to the Computational Hydrogen Electrode (CHE) approach,^[58] which does not alter the shape of the reaction profile.

Supporting Information

The Supporting Information is available free of charge.

Author Contributions

GV and MSG jointly conceived the work, while GV coordinated the research tasks. VR, FM, VB, and MSG prepared and characterized catalysts, with assistance from MB. VR performed all catalytic experiments. GB performed XPS analysis. YPI and GD performed microscopy analyses. GDL and GP performed DFT calculations. GV and GDL wrote the manuscript, with contributions from all coauthors.

Acknowledgements

FM thanks Birla Carbon for funding. GP acknowledges funding from the Italian Ministry of Education, University and Research (PRIN Project 20179337R7) and by the European Cooperation in Science and Technology (COST) Action 18234. GV acknowledges funding from the European Commission Horizon Europe programme (grant agreement 101057430, SusPharma). The authors thank the Paul Scherrer Institute (Switzerland) for XAS analyses.

Conflict of Interests

The authors declare no competing interests.

Data Availability Statement

All the data supporting the findings of this study are available within the article and its Supporting Information and also from the corresponding authors upon reasonable request.

Keywords: single-atom catalysis · graphite nanoplatelets · functional carbon materials · cross-coupling chemistry · covalent adducts

- [1] C. Zhu, H. Yue, J. Jia, M. Rueping, *Angew. Chem. Int. Ed.* **2021**, *60*, 17810–17831.
- [2] T. Tian, Z. Li, C.-J. Li, *Green Chem.* **2021**, *23*, 6789–6862.
- [3] K. L. Jensen, E. A. Standley, T. F. Jamison, *J. Am. Chem. Soc.* **2014**, *136*, 11145–11152.
- [4] E. Bisz, M. Szostak, *ChemSusChem* **2018**, *11*, 1290–1294.
- [5] M. B. Gawande, A. Goswami, F.-X. Felpin, T. Asefa, X. Huang, R. Silva, X. Zou, R. Zboril, R. S. Varma, *Chem. Rev.* **2016**, *116*, 3722–3811.
- [6] P. L. Pant, G. S. Shankarling, *New J. Chem.* **2018**, *42*, 13212–13224.
- [7] Y. Yuan, I. Thomé, S. H. Kim, D. Chen, A. Beyer, J. Bonnamour, E. Zuidema, S. Chang, C. Bolm, *Adv. Synth. Catal.* **2010**, *352*, 2892–2898.
- [8] R. Cano, D. J. Ramón, M. Yus, *J. Org. Chem.* **2011**, *76*, 654–660.
- [9] S. Sadeghi, M. Jafarzadeh, A. Reza Abbasi, K. Daasbjerg, *New J. Chem.* **2017**, *41*, 12014–12027.
- [10] T. R. Gordon, M. Cargnello, T. Paik, F. Mangolini, R. T. Weber, P. Fornasiero, C. B. Murray, *J. Am. Chem. Soc.* **2012**, *134*, 6751–6761.
- [11] B. Loges, A. Boddien, H. Junge, M. Beller, *Angew. Chem. Int. Ed.* **2008**, *47*, 3962–3965.
- [12] C. Copéret, M. Chabanas, R. Petroff Saint-Arroman, J.-M. Basset, *Angew. Chem. Int. Ed.* **2003**, *42*, 156–181.
- [13] B. Han, Y. Guo, Y. Huang, W. Xi, J. Xu, J. Luo, H. Qi, Y. Ren, X. Liu, B. Qiao, T. Zhang, *Angew. Chem. Int. Ed.* **2020**, *59*, 11824–11829.
- [14] A. Kumar, A. Kumar, V. Krishnan, *ACS Catal.* **2020**, *10*, 10253–10315.
- [15] Q. Liu, L. Wu, R. Jackstell, M. Beller, *Nat. Commun.* **2015**, *6*, 5933.
- [16] C. Krishnaraj, H. Sekhar Jena, L. Bourda, A. Laemont, P. Pachfule, J. Roeser, C. V. Chandran, S. Borgmans, S. M. J. Rogge, K. Leus, C. V. Stevens, J. A. Martens, V. Van Speybroeck, E. Breyneart, A. Thomas, P. Van Der Voort, *J. Am. Chem. Soc.* **2020**, *142*, 20107–20116.
- [17] M. B. Gawande, P. Fornasiero, R. Zboril, *ACS Catal.* **2020**, *10*, 2231–2259.
- [18] S. Navarro-Jaén, M. Virginie, J. Bonin, M. Robert, R. Wojcieszak, A. Y. Khodakov, *Nat. Chem. Rev.* **2021**, *5*, 564–579.
- [19] F. Chen, X. Jiang, L. Zhang, R. Lang, B. Qiao, *Chin. J. Catal.* **2018**, *39*, 893–898.
- [20] J.-S. Chen, A. N. Vasiliev, A. P. Panarello, J. G. Khinast, *Appl. Catal. A* **2007**, *325*, 76–86.
- [21] Y.-P. Zhang, A.-H. Shi, Y.-S. Yang, C.-L. Li, *Chin. Chem. Lett.* **2014**, *25*, 141–145.
- [22] V. Magné, T. Garnier, M. Danel, P. Pale, S. Chassaing, *Org. Lett.* **2015**, *17*, 4494–4497.
- [23] E. Akhavan, S. Hemmati, M. Hekmati, H. Veisi, *New J. Chem.* **2018**, *42*, 2782–2789.
- [24] V. V. Singh, A. K. Singh, *ACS Appl. Nano Mater.* **2018**, *1*, 2164–2174.
- [25] H. Q. Ha, H. T. D. Nguyen, T. H. M. Pham, V. T. Pham, T. Truong, *Catal. Commun.* **2018**, *117*, 79–84.
- [26] J. J. Leung, J. A. Vigil, J. Warnan, E. Edwardes Moore, E. Reisner, *Angew. Chem. Int. Ed.* **2019**, *58*, 7697–7701.
- [27] B. Reuillard, J. Warnan, J. J. Leung, D. W. Wakerley, E. Reisner, *Angew. Chem. Int. Ed.* **2016**, *55*, 3952–3957.
- [28] S. Campisi, C. Chan-Thaw, A. Villa, *Appl. Sci.* **2018**, *8*, 1159.
- [29] C. A. Campos-Roldán, G. Ramos-Sánchez, R. G. Gonzalez-Huerta, J. R. Vargas García, P. B. Balbuena, N. Alonso-Vante, *ACS Appl. Mater. Interfaces* **2016**, *8*, 23260–23269.
- [30] M. C. Román-Martínez, D. Cazorla-Amorós, A. Linares-Solano, C. S.-M. De Lecea, H. Yamashita, M. Anpo, *Carbon* **1995**, *33*, 3–13.
- [31] J.-M. Nhut, L. Pesant, J.-P. Tessonnier, G. Winé, J. Guille, C. Pham-Huu, M.-J. Ledoux, *Appl. Catal. A* **2003**, *254*, 345–363.
- [32] J.-S. Ye, X. Liu, H. F. Cui, W.-D. Zhang, F.-S. Sheu, T. M. Lim, *Electrochem. Commun.* **2005**, *7*, 249–255.
- [33] V. Datsyuk, M. Kalyva, K. Papagelis, J. Parthenios, D. Tasis, A. Siokou, I. Kallitsis, C. Galiotis, *Carbon* **2008**, *46*, 833–840.
- [34] M. Li, S. Ishihara, M. Akada, M. Liao, L. Sang, J. P. Hill, V. Krishnan, Y. Ma, K. Ariga, *J. Am. Chem. Soc.* **2011**, *133*, 7348–7351.
- [35] V. Barbera, A. Bernardi, A. Palazzolo, A. Rosengart, L. Brambilla, M. Galimberti, *Pure Appl. Chem.* **2018**, *90*, 253–270.
- [36] M. Galimberti, V. Barbera, S. Guerra, A. Bernardi, *Rubber Chem. Technol.* **2017**, *90*, 285–307.
- [37] M. Galimberti, V. Barbera, S. Guerra, L. Conzatti, C. Castiglioni, L. Brambilla, A. Serafini, *RSC Adv.* **2015**, *5*, 81142–81152.
- [38] J. Díaz, G. Paolicelli, S. Ferrer, F. Comin, *Phys. Rev. B* **1996**, *54*, 8064–8069.
- [39] T. Zhang, X. Nie, W. Yu, X. Guo, C. Song, R. Si, Y. Liu, Z. Zhao, *iScience* **2019**, *22*, 97–108.
- [40] E. Cano, M. F. López, J. Simancas, J. M. Bastidas, *J. Electrochem. Soc.* **2001**, *148*, E26.
- [41] V. A. M. Brabers, *Mater. Res. Bull.* **1983**, *18*, 861–868.
- [42] N. S. McIntyre, S. Sunder, D. W. Shoesmith, F. W. Stanchell, *J. Vac. Sci. Technol.* **1981**, *18*, 714–721.
- [43] J. F. Moulder, W. F. Stickle, P. E. Sobol, K. D. Bomben, *Handbook of X-Ray Photoelectron Spectroscopy*, Perkin-Elmer Corporation, Eden Prairie, Minnesota, **1992**.
- [44] M. T. M. Koper, *J. Solid State Electrochem.* **2016**, *20*, 895–899.
- [45] G. Di Liberto, L. A. Cipriano, G. Pacchioni, *J. Am. Chem. Soc.* **2021**, *143*, 20431–20441.
- [46] G. Berti, A. Calloni, A. Brambilla, G. Bussetti, L. Duò, F. Ciccacci, *Rev. Sci. Instrum.* **2014**, *85*, 073901.
- [47] G. Kresse, J. Hafner, *Phys. Rev. B* **1993**, *47*, 558–561.
- [48] J. P. Perdew, K. Burke, M. Ernzerhof, *Phys. Rev. Lett.* **1996**, *77*, 3865–3868.
- [49] G. Kresse, D. Joubert, *Phys. Rev. B* **1999**, *59*, 1758–1775.
- [50] P. E. Blöchl, *Phys. Rev. B* **1994**, *50*, 17953–17979.
- [51] S. Grimme, J. Antony, S. Ehrlich, H. Krieg, *J. Chem. Phys.* **2010**, *132*, 154104.

- [52] S. Grimme, S. Ehrlich, L. Goerigk, *J. Comput. Chem.* **2011**, *32*, 1456–1465.
- [53] J. K. Nørskov, T. Bligaard, A. Logadottir, J. R. Kitchin, J. G. Chen, S. Pandelov, U. Stimming, *J. Electrochem. Soc.* **2005**, *152*, J23.
- [54] K. Chan, C. Tsai, H. A. Hansen, J. K. Nørskov, *ChemCatChem* **2014**, *6*, 1899–1905.
- [55] F. Calle-Vallejo, M. D. Pohl, D. Reinisch, D. Loffreda, P. Sautet, A. S. Bandarenka, *Chem. Sci.* **2017**, *8*, 2283–2289.
- [56] R. Shang, S. N. Steinmann, B.-Q. Xu, P. Sautet, *Catal. Sci. Technol.* **2020**, *10*, 1006–1014.
- [57] J. D. Cox, D. D. Wagman, V. A. Medvedev, *CODATA - Key Values for Thermodynamics*, Hemisphere Publishing Corp., New York, **1989**.
- [58] J. K. Nørskov, J. Rossmeisl, A. Logadottir, L. Lindqvist, J. R. Kitchin, T. Bligaard, H. Jónsson, *J. Phys. Chem. B* **2004**, *108*, 17886–17892.

Manuscript received: October 20, 2023
Revised manuscript received: December 1, 2023
Accepted manuscript online: December 5, 2023
Version of record online: January 2, 2024